The Universality of Power Law Slopes in the Solar Photosphere and Transition Region Observed with HMI and IRIS

Markus J. Aschwanden

Lockheed Martin, Solar and Astrophysics Laboratory (LMSAL), Advanced Technology Center (ATC), A021S, Bldg.252, 3251 Hanover St., Palo Alto, CA 94304, USA; e-mail: aschwanden@lmsal.com

and

Nived Vilangot Nhalil

Armagh Observatory and Planetarium, College Hill, Armagh BT61 9DG, UK

ABSTRACT

We compare the size distributions of *self-organized criticality (SOC)* systems in the solar photosphere and the transition region, using magnetogram data from *Helioseismic and Magnetic Imager (HMI)* and *Interface Region Imaging Spectrograph (IRIS)* data. For each dataset we fit a combination of a Gaussian and a power law size distribution function, which yields information on four different physical processes: (i) photosopheric granulation convection dynamics (explaining the Gaussian random noise distribution in IRIS data); (ii) spicular plage events in the transition region (explaining the power law size distribution in IRIS data); (iii) salt-and-pepper small-scale magnetic structures (explaining the random noise distributions in HMI magnetograms); and (iv) magnetic reconnection processes in flares and nanoflares (explaining the power law size distribution in HMI data). We find a high correlation (CCC=0.97) between IRIS and HMI data. Datasets with magnetic flux balance are found to match the SOC-predicted power law slope $\alpha_F = 1.80$ for mean fluxes, which confirms the universality of SOC-inferred flux size distributions, and agrees with the results of Parnell et al. (2009), $\alpha_F = 1.85 \pm 0.14$.

Subject headings: methods: statistical — fractal dimension — Sun: transition region — solar granulation — solar photosphere —

1. INTRODUCTION

The atmospheric structure of the Sun consists of the photospheric layer on the solar surface, the chromosphere, the transition region, the corona, and solar wind regions, which all host different physical processes, characterized by the electron density, the electron temperature, and the magnetic field strength. In this study we sample very diverse temperature structures, from $T_e \approx 5800$ K observed in photospheric magnetograms with the *Helioseismic and Magnetic Imager (HMI)*, to $T_e \approx 10^4 - 10^6$ K, observed in Slitjaw images (SJI) of the 1400 Å channel of IRIS, which are dominated by the Si IV 1394 Å and 1403 Å resonance line, and form in the transition region (Rathore and Carlsson 2015; Rathore et al. 2015). Due to this huge temperature range, different physical processes are dominant in the various temperature regimes (Gallagher et al. 1998; Warren et al. 2016), and thus we do not know *a priori* whether the concept of *self-organized criticality (SOC)* systems is applicable (Aschwanden 2011; 2014; 2016; McAteer et al. 2016; Warren et al. 2016). More specifically, we want to understand the functional shapes of observed occurrence frequency (size) distributions, and whether they exhibit power law function (slopes) with universal validity in different temperature and wavelength regimes.

There is an ongoing debate on the functional form of size distributions in avalanching SOC processes, such as: a power law function, a log-normal distribution (Verbeeck et al. 2019), a Pareto distribution (Hosking and Wallis 1987), a Lomax distribution (Lomax 1954; Giles et al. 2011), or a Weibull distribution (Weibull 1951), for instance. Since all these functional forms are close to a power law function on the right-hand side of the size distribution, which is also called the "fat-tail", various linear combinations of these functional forms have been found to fit the observed size distributions to a comparable degree (Munoz-Jaramillo et al. 2015). In this study we use a combination of (Gaussian) linear random and (power law) nonlinear random structures. The linear (Gaussian) component describes the granulation dynamics (visible in IRIS data), as well as the salt-and-pepper structure (visible in HMI magnetograms). On the other side, the nonlinear power-law component may be produced by the spicular dynamics (visible in IRIS data), or by magnetic reconnection dynamics of small-scale features and nanoflares (visible in HMI magnetograms). Gaussian distributions have been tested with Yohkoh soft X-ray data (Katsukawa and Tsuneta 2001). Lognormal distributions, which are closest to our Gaussian-plus-power-law method used here, have been previously studied for Quiet-Sun FUV emission (Fontenla et al. 2007), solar flares (Verbeek et al. 2019), the solar wind (Burlaga and Lazarus 2000), accretion disks (Kunjaya et al. 2011), and are discussed also in Ceva and Luzuriaga (1998), Mitzenmacher (2004), and Scargle (2020).

There are at least two approaches to model SOC systems: (i) the microscopic concept that is based on avalanches driven by next-neighbor interactions in a lattice grid (Bak et al. 1987; Bak et al. 1988; Bak 1996), pioneered for solar flares by Lu and Hamilton (1991); and (ii) the macroscopic concept, where scaling laws and correlations between SOC parameters determine the statistical size distributions (Aschwanden 2012; 2016; 2022a), and waiting time distributions. A new aspect of this study is the invention of a single-image algorithm to derive approximate size distributions $N(F) \propto F^{-\alpha_F}$. One of our tests consists of comparing the slope α_F with the SOC-predicted value, i.e., $\alpha_F = 1.80$, which agrees also with observations of a more than the five decades extending size distribution inferred by Parnell et al. (2009), i.e., $\alpha_F = 1.85 \pm 0.14$. Another crucial test is the power law slope α_E of nanoflare energies, which is decisive for testing the viability of coronal heating energetics (Hudson 1991; Krucker and Benz 1998; Vilangot Nhalil et al. 2020; Aschwanden 2022b).

The content of this paper includes data analysis (Section 2), a discussion (Section 3), and conclusions (Section 4).

2. DATA ANALYSIS

When we observe solar emission at *near ultra-violet (NUV)* and *far ultra-violet (FUV)* wavelengths, we may gather photons from photospheric granulation structures (granules), as well as from spicules in plages in the transition region (at formation temperatures of $T_e \approx 10^4 - 10^6$). Consequently, we have to deal with multiple size distribution functions, which may include linear random processes (Gaussian noise) and/or nonlinear avalanche processes with power law distribution functions, also known as "fat-tail" distribution functions, which occur natually in *self-organized criticality (SOC)* systems.

2.1. Definitions of Flux Distributions

In the following we attempt to model event statistics with a combination of (i) a Gaussian distribution (originating from random processes, such as granular convection), and (ii) a power law distribution, e.g., created by spicular activity in the transition region, (Fig. 1). The Gaussian noise is defined in the standard way,

$$N(F)\ dF = N_0 \exp \left(- \frac{(F - F_0)^2}{2 \sigma_F^2} \right)\ dF\ , \tag{1}$$

where F is the flux averaged over the duration of an event (measured here at a wavelength of 1400 Å), $N(F)$ is the number of observed structures, F_0 is the mean value, σ_F is one standard deviation, and N_0 is the normalized number of events accumulated over time and area.

The second distribution we employ in our analysis is a power law distribution function, which is defined in the simplest way by,

$$N(F)\ dF = N_0 \left(\frac{F}{F_0} \right)^{-\alpha_F}\ dF\ , \tag{2}$$

where α_F is the power law slope of the relevant part of the distribution function.

The flux $F(t)$ of an event at time t is defined for IRIS data by,

$$F_{\rm IRIS}(t) = \frac{4\ \pi\ f(t)\ E_\lambda\ k}{A(t)\ \Omega}, \quad [{\rm erg\ cm^{-2} s^{-1}}] \tag{3}$$

where $f(t)$ is the mean observed flux at time (t) in DN/s (data number per second), E_λ is the energy of the photon, k is the factor that converts the DN to the number of photons, Ω is the *slit-jaw image (SJI)* in steradian, A [$\rm cm^{-2}$] is the area, and the background is subtracted (Vilangot Nhalil et al. 2020). In order to convert IRIS-observed fluxes into a SOC-inferred fluxes F, which has the physical units of [erg $\rm s^{-1}$]. spatial integration and temporal averaging is required,

$$F_{SOC} = \frac{\int_t^{t+T} F_{\rm IRIS}(t)\ A(t)\ dt}{T}, \quad [{\rm erg\ s^{-1}}]\ . \tag{4}$$

2.2. Analysis of IRIS Data

The 12 analyzed 1400 Å SJI images $F(x,y)$ of IRIS are shown in Fig. 2, which are identical in time and FOV (field-of-view) with those of Vilangot Nhalil et al. (2020), and are also identical with those used in the study on fractal dimension measurements (Aschwanden and Vilangot Nhalil 2022). The 12 IRIS maps shown in Fig. 2 have the following color code: The Gaussian distribution with values $F(x,y) < F_{thr}$ below a threshold of $F_{thr} = F_{avg} + F_{sig}$ is rendered with orange-to-red colors, while the power law function with the fat-tail $F(x,y) > F_{thr}$ is masked out with white color. In other words, all the orange-to-red regions in the IRIS maps visualize the locations of linear random noise (produced by granulation dynamics), while the white regions mark the location of SOC-driven nonlinear avalanches (probably produced by spicular dynamics in the transition region). An even crispier representation of the spicular component $F(x,y) > P_{thr}$, is displayed with a black-and-white rendering (Fig. 3), where black depicts locations with a power law distribution, and white demarcates locations with a Gaussian distribution

The information content of an IRIS image can be described with a 2-D array of flux values $F(x,y)$ at a given time t, or alternatively with a 1-D histogram $N(F)$. From the histogram $N(F)$ we calculate the average value F_{avg} and the standard deviation $\pm F_{sig}$, which corresponds to the Gaussian function, with a peak at F_0 and a standard deviation $F_{sig} = (F_2 - F_0)$ in Fig. (1) top panel. These averages and standard deviations, as well as the maximum flux values F_{max} [DN/s] are listed in Table 1. We see that the maximum flux values vary from $F_{max} = 26$ to 501 *DN/s*. Since we want to fit a two-component distribution function (i.e., with a Gaussian and a power law), we need to introduce a separator between the two distributions, which we choose to be one standard deviation above the average (see Fig. 1). We fit then both distribution functions (Eqs. 1 and 2) separately, the Gaussian function in the range of $[F_1, F_2]$, and the power law function in the range of $[F_2, F_3]$, as depicted in Fig. 1. We are fitting the distribution functions with a standard Gaussian fit method, and with a standard linear regression fit for the logarithmic flux function. Note that the power law function $N(S)$ appears to be a straight line in a logarithmic display only (Fig. 1 bottom panel), i.e., log(N)-log(S), but not in a linear representation (Fig. 1 top panel), i.e., lin(N)-lin(S), as used here.

The results of the fitting of the observed histograms are shown for all 12 datasets in Fig. (4), where the Gaussian fit is rendered with a blue color, and the power law fit with a red color. We see that our two-component model for the distribution function does produce acceptable fits to all analyzed IRIS data (histograms in Fig. 4), at least in the left half of the histograms.

If we would assume that all fluxes are generated by linear random noise, we would not be able to fit the nonlinear data at all. Obviously, we would under-predict most of the fluxes substantially (blue dashed curves in Fig. 4), which underscores that the "fat-tail" power law function, a hallmark of SOC processes, is highly relevant for fitting the observed IRIS 1400 Å data here.

In a next step we investigate the numerical values of the power law slopes α_F of the flux distribution parameters F, which are listed in the third column of Table 1. At a first glance, it appears that these values vary wildly in a range of $\alpha_F = 0.55$ to 2.15. However, Vilangot Nhalil et al. (2020) classified the 12 analyzed datasets into 4 cases containing a sunspot, and 8 cases containing plages in the transition region without sunspots. From this bimodal behavior it was concluded that the power law index of the energy distribution is larger in plages ($\alpha_E > 2$), compared with sunspot-dominated active regions ($\alpha_E < 2$), (Vilangot Nhalil et al. 2020). In our investigation here, the 4 cases with sunspots exhibit substantially flatter power law slopes α_F (except #3), which indicates that sunspot-dominant distributions are indeed significantly different from those without sunspots (Table 1). Actually, we find an even better predictor of this bimodal behavior, by using the maximum flux F_{max} (Column 6 in Table 1). We find that flux distributions $N(F) \propto F^{-\alpha_F}$ with maximum fluxes less than $F_{max} \lesssim 50$ [DN/s] exhibit a power law value of

$$\alpha_F^{obs} \approx 1.67 \pm 0.14, \quad F_{max} < 50 \text{ DN/s} \ , \tag{5}$$

which includes the five datasets #6, 7, 8, 9, 11. In contrast, the seven other datasets #1, 2, 3, 4, 5, 10, 12 have consistently higher maximum values, $F_{max} \gtrsim 50$ DN/s. Instead of using the maximum values F_{max}, we can also use the average fluxes F_{avg} and find the same bimodal behavior.

Even more significant is that this power law value is consistent with the theoretical prediction of the power law slopes (Aschwanden 2012; 2016; 2022a),

$$\alpha_{\rm F,SOC} = \frac{9}{5} = 1.80 \ . \tag{6}$$

Thus we can conclude that flux distributions have a power law slope that agrees with the theoretial prediction for small maximum fluxes, while distributions with large fluxes or with sunspots display flatter slopes. Apparently, more complex spatial structures produce flatter slopes.

2.3. Avalanche Detection Approximations

The standard method to sample size distributions $N(F)$ of SOC avalanches is generally carried out by an algorithm that detects an avalanche event above some given threshold $F > F_{thr}$, traces its spatial and temporal evolution, and determines the time-evolving envelope of the saturated avalanche. This has been accomplished for the same 12 IRIS datasets in the study of Vilangot Nhalil et al. (2020). Because the development of an automated feature recognition code is a complex and time-consuming task and needs extensive testing, we explore here two new methods that are much simpler to apply and require much less data to determine the underlying power law slopes α_F.

Our Method 1 samples all pixels of the 12 IRIS maps $F(x_i, y_j, t_i), i = 0, ..., N_x, j = 0, ..., N_y, k = 1, ..., 12$, Essentially, this strategy assumes that every single pixel represents an avalanche, differing from each other by the peak flux $F(x_i, y_j, t_k)$ only. This Method 1 was used in the calculations of the values $\alpha_{\rm F1}$ listed in Table 1.

In order to test the robustness of Method 1 we conceive a Method 2, where only those pixels were sampled that represent a local peak relative to the 4 next neighbors,,

$$F(x_i, y_j) > [F(x_{i-1}, y_j), F(x_{i+1}, y_j), F(x_i, y_{j-1}), F(x_i, y_{j+1}] \ . \tag{7}$$

From the 12 IRIS maps and the corresponding power law slopes α_F we compare the values of the power law slopes for Method 1 and Method 2 in Fig. 5, from which we find a high cross-correlation coefficient of CCC=0.99, ignoring one outlier event (#3). A linear regression fit between the two methods yields (Fig. 5),

$$\alpha_{\rm F2} = 0.14 + 1.32 \times \alpha_{\rm F1} \ . \tag{8}$$

so the two distributions of power law slopes are almost proportional, except for a slight bias in the slope. This deviation stems from the different approximations of avalanche geometries, one using all pixels (Method 1), and one using the peak pixels only (Method 2). We can consider Method 1 as an upper limit, and Method 2 as a lower limit of the “true” size distribution, i.e., ($\alpha_{\rm F2} < \alpha_{\rm F} < \alpha_{\rm F1}$).

2.4. HMI Magnetogram Analysis

In order to test the universality of the results we repeat the same analysis for 12 coincident HMI magnetograms onboard the Solar Dynamics Observatory (SDO), which have simultaneous times and identical spatial field-of-views. The 12 analyzed HMI images are shown in Fig. 6, where black features indicate negative magnetic polarity, and white features indicate positive magnetic polarity. We see sunspots in at least 4 magnetograms (#1, 2, 3, 10), with sunspots having a negative magnetic polarity (#1, 2), and two cases with positive magnetic polarity (#3, 10). All 12 magnetograms show mixed polarities, but some are heavily unbalanced (#1-5, 10-12).

We quantify the magnetic flux balance with the ratio q_{pos},

$$q_{pos} = \left(\frac{\sum_{pos} F_{ij}}{\sum_{pos} F_{ij} + |\sum_{neg} F_{ij}|} \right) \ . \tag{9}$$

If the magnetic flux (line-of-sight) component is well-balanced, we would expect a value of $q_{pos} = 0.5$, assuming $\sum_{pos} = \sum_{neg}$. Only 4 cases have approximately balanced fluxes (#6, 7, 8, 9), namely $q_{pos} =$

$[0.44, 0.43, 0.38, 0.44]$, while the other 6 cases have large flux imbalances, from $q_{pos} = 0.04$ to 0.99 (Table 2 and Fig. 7). The associated power law slopes of the 4 well-balanced cases are $\alpha_F = [1.57, 1.71, 1.89, 1.81] = 1.75 \pm 0.12$ which coincides with those cases that have a power law slope close to the theoretical SOC-prediction of $\alpha_F \approx 1.80$ (Aschwanden 2012; 2016; 2022a).

We analyze the HMI data in the same way as the IRIS data, by fitting joint Gaussian distributions (blue curves in Fig. 7) and power law distribution functions (red curves in Fig. 7), which clearly show a "fat-tail" feature that is far in excess of the Gaussian function (blue dashed curves in Fig. 7). We compare the power law slopes α_F obtained with the two completely different datasets from IRIS and HMI in Fig. 8, using the all-pixels Method 1. The two datasets are found to be highly correlated (with CCC=0.97, if we ignore the outlier #3). The scaling of the two correlated datasets can be described by a linear regression fit,

$$\alpha_{\rm F,HMI} = 0.71 + 0.64 \ \alpha_{\rm F,IRIS} \ , \tag{10}$$

which indicates an (unknown) more complex scaling law. Nevertheless, the power law slopes α_F are concentrated in two regimes, one that is consistent with our theoretical SOC prediction of $\alpha_{\rm F,IRIS} = \alpha_{\rm F,HMI} \approx 1.80$, while a second cluster is centered around $\alpha_{\rm F,IRIS} \approx 0.6 - 1.0$ and $\alpha_{\rm F,HMI} \approx 1.0 - 1.4$ (Fig. 8). In essence, we find 5 datasets (# 6, 7, 8, 9, 11) that are consistent with the SOC prediction for events with well-balanced flux $q_{pos} \approx 0.5$, while a second group cannot reproduce the SOC model, but can be characterized with large unblanced magnetic fluxes (# 1, 2, 3, 4, 5, 10, 12). Apparently, the magnetic flux balance is decisive whether the calculated power law slopes are universally consistent with SOC models or not.

The physical interpretation of the IRIS data is, of course, different for the HMI data. In the previous analysis of IRIS data we interpreted the linear random distribution due to the granulation dynamics, and the nonlinear avalanche statistics in terms of SOC-controlled power law functions due to spicules in the transition region. In contrast, using the HMI data, which provides the magnetic field line-of-sight component B_z, we can interpret the statistics of linear random distributions in terms of "salt-and-pepper" small-scale magnetic fields in the photosphere, and the nonlinear avalanche statistics in terms of SOC-controlled magnetic reconnection processes in nanoflares and larger flares (Table 3). Note that the two parameters $\alpha_{\rm F,IRIS}$ amd $\alpha_{\rm F,HMI}$ are observed independently from different spacecraft, as well as in markedly different wavelength bands, i.e., $\lambda \approx 1400$ Å for IRIS, and $\lambda = 6173$ Å for HMI/SDO magnetograms, which measures the mean flux F from the line-of-sight magnetic field component $B_z(x, y)$. Despite of the very different instruments and wavelengths, the power law slope α_F of the mean flux appears to be universally valid and consistent with the theoretical SOC prediction for datasets with approximate magnetic flux balance (Fig. 8). However we learned that the magnetic flux balance and the absence of sunspots represent additional requirements to warrant the universality of the SOC slopes. This yields a testable prediction: If the field-of-view of each HMI magnetogram is readjusted so that the enclosed magnetic flux becomes more balanced and no sunspot appears in the FOV, the power law slope is expected to approach the theoretical universal value of $\alpha_{\rm F,IRIS} \approx \alpha_{\rm F,HMI} \approx 1.80$.

3. DISCUSSION

In the following we discuss two linear random processes (convective granulation, salt-and-pepper small-scale scale magnetic features), and two nonlinear random processes (spicular dynamics, magnetic reconnection, flaring, and nanoflaring), which relate to each other as depicted in Table 3.

3.1. Magnetic Flux Distribution

The most extensive statistical study on the size distribution of magnetic field features on the solar surface has been undertaken by Parnell et al. (2009). Combining magnetic field data from three instruments (SOT/Hinode, MDI/NFI, and MDI/FD on SOHO, a combined occurrence frequency size distribution was synthesized that extends over five decades, in the range of $\Phi = 2 \times 10^{17} - 10^{23}$ Mx (Parnell et al. 2009),

$$N(\Phi) \propto (\Phi_0)^{-1.85 \pm 0.14} \quad [\mathrm{Mx}^{-1} \mathrm{cm}^{-2}] \ , \tag{11}$$

where the magnetic flux Φ is obtained from integration of the magnetic field $B(x, y)$ over a thresholded area $A = \int \ dx \ dy$,

$$\Phi = \int B(x, y) \ dx \ dy \quad [\mathrm{Mx}] \ . \tag{12}$$

If we equate the magnetic (feature) flux Φ with the mean flux F of an event in standard SOC models, we predict a power law slope of (Aschwanden 2012; 2016; 2022a),

$$\alpha_{\mathrm{F,SOC}} = 1 + \frac{(d-1)}{(\gamma D_V)} = \frac{9}{5} = 1.80 \ , \tag{13}$$

which agrees well with the result (Eq. 11) observed by Parnell et al. (2009). A lower value was found from cellular automaton simulations, $N(\Phi) \approx \Phi^{-1.5 \pm 0.05}$ (Fragos et al. 2004), where flux emergence is driven by a percolation rule, similar to the percolation model of Seiden and Wentzel (1996), or Balke et al. (1993). Mathematical models have been developed to model the percolation phenomenon, based on combinatorial and statistical concepts of connectedness that exhibit universality in form of powerlaw distributions.

3.2. Universality of SOC Size Distributions

Power-law-like size distributions are the hallmark of self-organized criticality systems. Statistical studies in the past have collected SOC parameters such as length scales L, time scales T, peak flux rates P, mean fluxes F, fluences and energies $E = F \times T$, mono-fractal and multi-fractal dimensions (Mandelbrot 1977), in order to test whether the theoretically expected power law size distributions, or the power law slopes of waiting times, agree with the observed distributions (mostly observed in astrophysical systems). The universality of SOC models (Aschwanden 2012; 2016; 2022a) is based on four scaling laws: the scale-free probability conjecture $N(L) \propto L^{-d}$, classical diffusion $L \propto T^{\beta/2}$, the flux-volume relationship $F \propto V^{\gamma}$, and the Euclidean scaling law, $P \propto L^{\gamma d}$, where $d = 3$ is the Euclidean dimension, $\beta \approx 1$ is the classical diffusion coefficient, $\gamma \approx 1$ the flux-volume proportionality, while $D_A = 3/2$ and $D_V = 5/2$ are the mean fractal dimensions in 2-D and 3-D Euclidean space. The standard SOC model is expressed in terms of these universal constants: $d = 3$, $\gamma = 1$, $\beta = 1$, and the mean fractal dimension $D_v = 5/2$. Consequently, the four basic scaling laws reduce to $N(L) \propto L^{-3}$, $L \propto T^{1/2}$, and $F \propto L^{2.5}$. Since we measure the mean flux F in this study, our main test of the universality of SOC models if formulated in terms of the flux-volume relationship $F \propto V^{\gamma}$, leading to the power law slope $\alpha_{\mathrm{F,SOC}} = 1.80$ (Eq. 13).

The SOC-inferred scaling laws hold for a large number of phenomena. This implies that our SOC formalism is universal in the sense that the statistical size distributions are identical for each phenomenon, displaying a universal power law slope of $\alpha_{\mathrm{F,SOC}} = 1.80$. When we conclude that the power law slope α_F is universal, the SOC model implies that the flux-volume proportionality ($\gamma \approx 1$) as well as the mean fractal dimension ($D_V \approx 2.5$, $d = 3$) are universal too.

3.3. Physical Processes in SOC Systems

Once we establish the self-consistency of power law slopes between theoretical (SOC) and observed size distributions, the next question is what physical processes are at work. We envision four different physical processes (Table 3): (i) photosopheric granulation dynamics (to explain the Gaussian random noise distribution in IRIS data); (ii) spicular plage events in the transition region (to explain the power law size distribution in IRIS data); (iii) salt-and-pepper small-scale magnetic structures (to explain the random noise distributions in HMI magnetograms); and (iv) magnetic reconnection proceses in flares and nanoflares (to explain the power law size distribution in HMI data). However, there are deviations from these rules. We found that the power law distributions are modified in the presence of sunspots, or when the magnetic flux is unbalanced. Under ideal conditions, the SOC scaling laws are fulfilled universally, independent of the wavelength or plasma temperature. Magnetic field data (from HMI/SDO) or $\lambda \approx 1400$ Å (from IRIS) produce emission in volumes that are proportional in the photosphere or transition zone, even when they are formed at quite different temperatures, i.e., $T_{\rm phot} \approx 5800$ K in the photosphere and $T_{\rm TR} \approx 10^4 - 10^6$ K in the transition region.

Another ingredient of the SOC model is the scale-free probability conjecture, i.e., $N(L) \propto L^{-d} = L^{-3}$, which cannot be uniquely linked to a particular physical process. Parnell et al. (2009) conclude that a combination of emergence, coalescence, cancellation, and fragmentation may possibly produce power law size distributions of spatial scales L. Alternative models include the turbulence, the magneto-chemistry equations (Schrijver et al. 1997), and Weibull distributions (Parnell 2002). Munoz-Jaramillo et al. (2015) study the best-fitting distribution functions for 11 different databases of sunspot areas, sunspot group areas, sunspot umbral areas, and magnetic fluxes. They find that a linear combination of Weibull and log-normal distributions fit the data best (Munoz-Jaramillo et al. 2015). Weibull and log-normal distributions combine two distribution functions, similar to our synthesis of a Gaussian-plus-power-law distribution.

A general physical scenario of a power law size distribution is the evolution of avalanches by exponential growth (Rosner and Vaiana 1978), with subsequent saturation (logistic growth) after a random time interval, which produces an exact power law function (Aschwanden et al. 1998). Our approach to model the size distribution of solar phenomena with two different functions, employing a Gaussian noise and a power law tail, reflects the duality of a linear and a nonlinear random component, in both the data from IRIS and HMI (Table 3). In summary, linear random components include granulation, super-granulation, and salt-and-pepper small-scale magnetic features, while nonlinear components include spicular avalanches and magnetic reconnection avalanches from nanoflares to large flares.

3.4. Granular Dynamics

The physical understanding of solar (or stellar) granulation has been advanced by numerical magneto-convection models and N-body dynamic simulations, which predict the evolution of small-scale (granules) into large-scale features (meso- or super-granulation), organized by surface flows that sweep up small-scale structures and form clusters of recurrent and stable granular features (Hathaway et al. 2000; Berrilli et al. 1998, 2005; Rieutord et al. 2008, 2010; Cheung and Isobe 2014; Martinez-Sykora et al. 2008). The fractal multi-scale dynamics has been found to be operational in the Quiet-Sun photosphere, in quiescent non-flaring states, as well as during flares (Uritsky et al. 2007, 2013; Uritsky and Davila 2012). A common origin of granulation and super-granulation network cells is assumed (Berrilli et al. 1998). The fractal structure of the solar granulation is obviously a self-organizing pattern that is created by a combination of subphotospheric magneto-convection and surface flows, which are turbulence-type phenomena. The spatial structure of photospheric granulation has also been explained in terms of a self-organization (SO) process (without criticality !), where order is created out of randomness (Aschwanden et al. 2018).

3.5. Spicular Dynamics

One prominent feature in the transition region is the phenomenon of *"moss"*, which appears as a bright dynamic pattern with dark inclusions, on spatial scales of $L \approx 1 - 3$ Mm, which has been interpreted as the upper transition region above active region plages, and below relatively hot loops (De Pontieu et al. 1999; 2014). Our measurement of structures in the IRIS 1400 Å channel is sensitive to a temperature range of $T_e \approx 10^4 - 10^6$ K, and thus is likely to include chromospheric and transition region phenomena such as: spicules II (De Pontieu et al. 2007), macro-spicules, dark mottles, dynamic fibrils, surges, miniature filament eruptions, etc. Theoretical models include the rebound shock model (Sterling and Hollweg 1988), pressure-pulses in the high atmosphere (Singh et al. 2019), Alfv'enic resonances (Sterling 1998), magnetic reconnection models for type II spicules (De Pontieu et al. 2007), ion-neutral collisional damping (De Pontieu 1999), leakage of global p-mode oscillations (De Pontieu et al. 2004), MHD kink waves (Zaqarashvili and Erdelyi 2009), vortical flow models (Kitiashvili et al. 2013), and magneto-convective driving by shock waves (De Pontieu et al. 2007).

The fact that we obtain a power law size distribution ($\alpha_F = 1.67 \pm 0.14$, Table 1), which is very similar to solar flares in general, $\alpha_{\rm F,SOC} = 1.80$, implies the universality of the SOC framework. Furthermore we find power law-like size distributions for spicular events, rather than a Gaussian distribution, which tells us that spicule events need to be modeled in terms of SOC-driven avalanches, instead of with Gaussian random distributions. The difference between linear and nonlinear random processes is the property of coherent growth, which results into exponential (or logistic) growth, after triggered by an instability. This does not happen for incoherent growth.

3.6. Salt-and-Pepper Magnetic Field

We interepret the random noise Gaussian distribution of magnetic fluxes in Quiet-Sun regions as small-scale magnetic field "pepper-and-salt" structures, also called *magnetic carpet* (Priest et al. 2002), where the black and white color in magnetograms corresponds to negative and magnetic polarity. According to our analysis, the magnetic flux has an average of $F_{avg} \approx 10 - 200$ DN/s, and a similar standard deviation of $F_{sigm} \approx 10 - 200$ DN/s (Table 1). The fact that we obtain two distinctly different size distributions (Gaussian vs. power law) indicates at least two different physical mechanisms, one being a linear random (Gaussian) process, the other one being a nonlinear (power law) avalanche process. The salt-and-pepper structure is generated apparently by a linear random process, rather than by an nonlinear avalanching process, according to our fits. This may constrain the origin of the solar magnetic field, being created by emergence, coalescence, cancellation, and/or fragmentation.

3.7. Magnetic Reconnection

The re-arrangement of the stress-induced solar magnetic field requires ubiquitous and permanent (but intermittent) magnetic reconnection processes on all spatial and temporal scales. Our study finds power law size distributions, with a slope of $\alpha_F = 1.75 \pm 0.12$ from HMI magnetograms, which is similar to flares in general (see Aschwanden et al. 2016 for a review of all wavelengths, gamma-rays, hard X-rays, soft X-rays, EUV, etc). This tells us that there is a strong correlation between the photospheric field (in HMI images) and the transition region (in IRIS images), as evident from the cross-correlation coefficient of CCC=0.97 shown in Fig. 8. The fractal multi-scale dynamics apparently operates in the quiet photosphere, in the quiescent non-flaring state, as well as during flares in active regions (Uritsky and Davila 2012).

4. CONCLUSIONS

Solar and stellar flares, pulsar glitches, auroras, lunar craters, as well as earthquakes, landslides, wildfires, snow avalanches, and sandpile avalanches are all driven by self-organized criticality (SOC), which predicts power law-like occurrence frequency (size) distributions and waiting time distribution functions. What is new in our studies of SOC systems is that we are now able to calculate the slope α_x of power law functions, which allows us to test SOC models by comparing the observed (and fitted) distribution functions with the theoretically predicted values. In this study we compare statistical distributions of SOC parameters from different wavelengths and different instruments (UV emission observed with IRIS and magnetograms with HMI). The results of our study are:

1. The histogrammed distribution of fluxes $N(F)$ obtained from an IRIS 1400 Å image, or from a HMI magnetogram, cannot be fitted solely by a Gaussian function, but requires a two-component function, such as a combination of a Gaussian and a power law function, i.e., a "fat-tail" extension above about one standard deviation. We define a separator between the two functions at one standard deviation and obtain power law slopes of $\alpha_F = 1.67 \pm 0.14$ from the IRIS data, and $\alpha_F = 1.75 \pm 0.12$ from the HMI data, which agree with the theoretical SOC prediction of $\alpha_F = 1.80$, and thus demonstrate universality across UV wavelengths and magnetograms. Moreover, it agrees with the five order of magnitude extending power law distribution sampled by Parnell et al. (2009), $\alpha_F = 1.85 \pm 0.14$.

2. The phenomenology of the 12 analyzed dataset consists of 4 active regions with sunspots, while the other 8 cases were selected in plage regions and in the Quiet-Sun. It turns out that regions with large average fluxes ($F_{avg} > 50$) DN/s, have a large unbalanced flux, and contain sunspots. Therefore, matching the theoretical SOC prediction requires magnetic flux balance and the absence of sunspots, in order to warrant universality of the flux power law distribution function.

3. We designed two algorithms that produce size distributions from a single image (e.g., from a UV image or a magnetogram), by sampling a histogram using all pixels (Method 1), or a histogram using only pixels with a local peak (Method 2). The two methods agree closely with each other (with a cross-correlation coefficient of CCC=0.99. One can consider Method 1 as an upper limit, and Method 2 as a lower limit to the "true" size distributions, i.e., ($\alpha_{\rm F2} < \alpha_{\rm F} < \alpha_{\rm F1}$). Both methods are computationally very fast and do not require any particular automated pattern recognition code.

4. We can interpret the analyzed size distributions in terms of four distinctly different physical processes: (i) photospheric granulation dynamics (explaining the Gaussian random noise distribution in IRIS

data); (ii) spicular plage events in the transition region (explaining the power law size distribution in IRIS data); (iii) salt-and-pepper small-scale magnetic structures (explaining the random noise distributions in HMI magnetograms); and (iv) magnetic reconnection processes in flares and nanoflares (explaining the power law size distribution in HMI data).

Future work may include: (i) testing of the SOC-predicted size distributions with power law slopes α_F for all available (mean) fluxes F (in HXR, SXR, EUV, etc.); (ii) testing the selection of different FOV sizes in the absence or existence of sunspots, and magnetic flux balance; (iii) testing and cross-comparing the approximations of the all-pixel (Method 1) and peak-pixel (Method 2). Ultimately these methods should help us to converge the numerical values in SOC models.

Acknowledgements: We acknowledge constructive comments of reviewers and stimulating discussions (in alphabetical order) with Paul Charbonneau, Adam Kowalski, Karel Schrijver, Vadim Uritsky, and Nived Vilangot Nhalil. This work was partially supported by NASA contract NNX11A099G "Self-organized criticality in solar physics", NASA contract NNG04EA00C of the SDO/AIA instrument, and the IRIS contract NNG09FA40C to LMSAL.

References

Aschwanden, M.J., Dennis, B.R., and Benz, A.O. 1998, *Logistic avalanche processes, elementary time structures, and frequency distributions in solar flares*, ApJ 497, 972

Aschwanden, M.J. 2011, *Self-Organized Criticality in Astrophysics. The Statistics of Nonlinear Processes in the Universe*, ISBN 978-3-642-15000-5, Springer-Praxis: New York, 416p.

Aschwanden, M.J. 2012, *A statistical fractal-diffusive avalanche model of a slowly-driven self-organized criticality system*, A&A 539, A2, (15 p)

Aschwanden, M.J. 2014, *A macroscopic description of self-organized systems and astrophysical applications*, ApJ 782, 54

Aschwanden,M.J., Crosby,N., Dimitropoulou,M., Georgoulis,M.K., Hergarten,S., McAteer,J., Milovanov,A., Mineshige,S., Morales,L., Nishizuka,N., Pruessner,G., Sanchez,R., Sharma,S., Strugarek,A., and Uritsky, V. 2016, *25 Years of Self-Organized Criticality: Solar and Astrophysics* Space Science Reviews 198, 47-166.

Aschwanden, M.J., Scholkmann, F., Bethune, W., Schmutz, W., Abramenko,W., Cheung,M.C.M., Mueller,D., Benz,A.O., Chernov,G., Kritsuk,A.G., Scargle,J.D., Melatos,A., Wagoner,R.V., Trimble,V., Green,W. 2018, *Order out of randomness: Self-organization processes in astrophysics*, Space Science Reviews 214:55

Aschwanden, M.J. 2022a, *The fractality and size distributions of astrophysical self-organized criticality systems*, ApJ 934:33

Aschwanden, M.J. 2022b, *Reconciling power-law slopes in solar flare and nanoflare size distributions*, ApJL 934:L3

Aschwanden, M.J. and Vilangot Nhalil, N. 2022, *Interface region imaging spectrograph (IRIS) observations of the fractal dimension in the solar atmosphere*, Frontiers in Astronomy and Space Sciences, Manuscript ID 999329

Balke,A.C., Schrijver, C.J., Zwaan,C., and Tarbell,T.D. 1993, *Percolation theory and the geometry of photospheric magnetic flux concentrations*, Solar Phys. 143, 215.

Bak, P., Tang, C., and Wiesenfeld, K. 1987, *Self-organized criticality: An explanation of 1/f noise*, Physical Review Lett. 59(27), 381

Bak, P., Tang, C., and Wiesenfeld, K. 1988, *Self-organized criticality*, Physical Rev. A 38(1), 364

Bak, P. 1996, *How Nature Works. The Science of Self-Organized Criticality*, New York: Copernicus

Berrilli, F., Florio, A., and Ermolli, I. 1998, *On the geometrical properties of the chromospheric network*, Sol.Phys. 180, 29-45

Berrilli, F., Del Moro, D., Russo, S., et al. 2005, *Spatial clustering of photospheric structures*, ApJ 632, 677

Burlaga, L.F. and Lazarus, A.J. 2000, *Lognormal distributions and spectra of solar wind plasma fluctuations: Wind 1995-1998*, JGR 105, 2357

Ceva, H. and Luzuriaga, J. 1998, *Correlations in the sand pile model: From the log-normal distribution to self-organized criticality*, Physics Letters A 250, 275

Cheung, M.C.M. and Isobe, H. 2014, *Flux emergence (Theory)*, LRSP 11, 3.

De Pontieu, B. 1999, *Numerical simulations of spicules driven by weakly-damped Alfven waves I. WKB approach*, A&A 347, 696

De Pontieu, B., Berger, T.E., Schrijver, C.J., and Title, A.M. 1999, *Dynamics of transition region 'moss' at high time resolution.* Sol.Phys. 190, 419

De Pontieu, B., Erdelyi, R., and James, S.P. 2004, *Solar chromospheric spicules from the leakage of photospheric oscillations and flows*, Nature 430, 536

De Pontieu, B., Title, A.M., Lemen, J.R., Kushner, G.D., Akin, D.J., Allard, B., Berger, T., Boerner, P., 2014, The Interface Region Imaging Spectrograph (IRIS), Sol.Phys. 289, 2733

De Pontieu,B., McIntosh,S., Hansteen,V.H., Carlsson,M., Schrijver,C.J., et al. 2007, *A tale of two spicules: The impact of spicules on the magnetic chromosphere*, PASJ 59, S655

Fontenla, J.M., Curdt, W., Avrett, E.H., and Harder, J. 2007, *Log-normal intensity distribution of the quiet-Sun FUV continuum observed by SUMER*, A&A 468, 695

Fragos, T., Rantsiou, E., and Vlahos, L. 2004, *On the distribution of magnetic energy storage in solar active regions*, A&A 420, 719.

Gallagher, P.T., Phillips, K.J.H., Harra-Murnion, L.K., et al. 1998, *Properties of the Quiet Sun EUV network*, A&A 335, 733

Giles, D.E., Feng,H., and Godwin,R.T. 2011, *On the bias of the maximum likelihood estimator for the two-parameter Lomax distribution*, Econometrics Workshop Paper EWP1104, ISSN 1485

Hathaway, D.H., Beck, J.G., Bogart, R.S., et al. 2000, *The photospheric convection spectrum* SoPh 193, 299

Hosking, J.R.M. and Wallis, J.R. 1987, *Parameter and quantile estimation for the generalized Pareto distribution*, Technometrics, 29(3), 339

Hudson, H.S. 1991, *Solar flares, microflares, nanoflares, and coronal heating*, Sol.Phys. 133, 357

Katsukawa, Y. and Tsuneta, S. 2001, *Small fluctuation of coronal X-ray intensity and a signature of nanoflares*, ApJ 557, 343

Kitiashvili, I.N., Kosovichev, A.G., Lele, S.K., Mansour, N.N. and Wray, A.A. 2013, *Ubiquitous solar eruptions driven by magnetized vortex tubes*, ApJ 770, 37

Krucker, S. and Benz, A.O. 1998, *Energy distribution of heating processes in the quiet solar corona*, ApJ 501, L213

Kunjaya, C., Mahasena, P., Vierdayanti, K., and Herlie, S. 2011, *Can self-organized critical accretion disks generate a log-normal emission variability in AGN?*, ApSS 336, 455

Lomax, K.S. 1954, J. Am. Stat. Assoc. 49, 847

Lu, E.T. and Hamilton, R.J. 1991, *Avalanches and the distribution of solar flares*, ApJ 380, L89

Mandelbrot, B.B. 1977, *The Fractal Geometry of Nature.* W.H.Freeman and Company: New York

Martinez-Sykora, J., Hansteen,V., and Carlsson, M. 2008, *Twisted Flux Tube Emergence From the Convection Zone to the Corona*, ApJ 679, 871

McAteer,R.T.J., Aschwanden,M.J., Dimitropoulou,M., Georgoulis,M.K., Pruessner, G., Morales, L., Ireland, J., and Abramenko,V. 2016, *25 Years of Self-Organized Criticality: Numerical Detection Methods*, SSRv 198 217-266.

Mitzenmacher, M. 2004, *A brief history for generative models for power law and lognormal distributions*, Internet mathematics 1(2), 226

Munoz-Jaramillo, A., Senkpeil, R.R., Windmueller, J.C., Amouzou, E.C., et al. 2015, *Small-scale and Global Dynamos and the Area and Flux Distributions of Active Regions, Sunspot Groups, and Sunspots: A Multi-database Study*, ApJ 800, 48

Parnell, C.E. 2002, *Nature of the magnetic carpet - 1. Distribution of magnetic fluxes*, MNRAS 335/2, 398.

Parnell, C.E., DeForest, C.E., Hagenaar, H.J., Johnston, B.A., Lamb, D.A., and Welsch, B.T. 2009, *A Power-Law Distribution of Solar Magnetic Fields Over More Than Five Decades in Flux*, ApJ 698, 75-82

Priest,E.R., Heyvaerts, J.F., and Title, A.M. 2002, *A Flux-Tube Tectonics Model for Solar Coronal Heating Driven by the Magnetic Carpet*, ApJ 576, 533

Rathore, B. and Carlsson, M. 2015, *The Formation of IRIS Diagnostics. VI. The Diagnostic Potential of the C II Lines at 133.5 nm in the Solar Atmosphere*, ApJ 811, 80

Rathore, B., Carlsson, M., Leenaarts, J., De Pontieu B. 2015, *The Formation of Iris Diagnostics. VIII. Iris Observations in the C II 133.5 nm Multiplet*, ApJ 811, 81

Rieutord, M., Meunier, N., Roudier, T., et al. 2008, *Solar super-granulation revealed by granule tracking*, A&A 479, L17

Rieutord, M., Roudier, T., Rincon, F., 2010, *On the power spectrum of solar surface flows*, A&A 512, A4

Rosner, R., and Vaiana, G.S. 1978, *Cosmic flare transients: constraints upon models for energy storage and release derived from the event frequency distribution*, ApJ 222, 1104

Scargle, J.D. 2020, *Studies in astronomical time-series analysis. VII. An enquiry concerning nonlinearity, the rms-mean flux relation, and lognormal flux distributions*, ApJ 895, 90

Schrijver, C.J., Hagenaar, H.J., and Title, A.M. 1997 *On the patterns of the solar granulation and supergranulation*, ApJ 475, 328-337

Seiden, P.E. and Wentzel, D.G. 1996, *Solar active regions as a percolation phenomenon II.* ApJ 460, 522

Singh, B., Sharma, K., and Srivastava, A.K. 2019, *On modelling the kinematics and evolutionary properties of pressure=puls-driven impulsive solar jets*, Ann.Geophys. 37, 891

Sterling,A.C. and Hollweg,J.V. 1988, *The rebound shock model for solar spicules: Dynamics at long times* ApJ 327, 950

Sterling, A.C. 1998, *Alfvénic resonances on ultraviolet spicules*, ApJ 508, 916

Uritsky, V.M., Paczuski, M., Davila, J.M., and Jones, S.I. 2007, *Coexistence of self-organized criticality and intermittent turbulence in the solar corona*, Phys. Rev. Lett. 99(2), id. 025001

Uritsky, V.M., and Davila, J.M. 2012, *Multiscale Dynamics of Solar Magnetic Structures*, ApJ 748, 60

Uritsky, V.M., Davila, J.M., Ofman, L., and Coyner, A.J. 2013, *Stochastic coupling of solar photosphere and corona*, ApJ 769, 62

Verbeeck, C., Kraaikamp, E., Ryan, D.F., and Podladchikova, O. 2019, *Solar Flare Distributions: Lognormal Instead of Power Law?*, ApJ 884, 50

Vilangot Nhalil, N.V., Nelson, C.J., Mathioudakis, M., and Doyle, G.J. 2020, *Power-law energy distributions of small-scale impulsive events on the active Sun: results from IRIS*, MNRAS 499, 1385

Warren, H.P., Reep, J.W., Crump, N.A., and Simoes, P.J.A. 2016, *Transition region and chromospheric signatures of impulsive heating events. I. Observations*, ApJ 829:35

Weibull, W. 1951, *A statistical distribution function of wide applicability*, J. Appl. Mech 18(3) 293

Zaqarashvili, T.V. and Erdelyi, R. 2009, *Oscillations and waves in solar spicules*, SSRv 149, 355

Table 1: Results of 12 datasets obtained with IRIS 1400 Å, including the power law slope α_{F1} of the flux distribution, the maximum flux F_{max}, and fractal dimension D_A. Note that the power law slope α_F agrees with the theoretical prediction of $\alpha_F = 9/5 = 1.8$, whenver there is no sunspot and the maximum flux F_{max} amounts to less than a critical value of $F_{max} \lesssim 50$ DN/s. The values of α_{F1} in parenthesis indicate outliers.

Number Dataset IRIS #	Phenomenon 1400 Å	Power law slope fit $\alpha_{\rm F1}$	Agrees with prediction $\alpha_{\rm F1} \approx 1.8$	Average flux $F_{avg} \pm F_{sig}$ [DN/s]	Maximum flux F_{max} [DN/s]	Max.flux criterion < 50 DN/s	Fractal dimension D_A
1	Sunspot	(0.87±0.04)	NO	47± 73	121	NO	1.44
2	Sunspot	(0.85±0.01)	NO	77±112	190	NO	1.56
3	Sunspot	(2.15±0.07)	NO	129±113	243	NO	1.53
4	Plage	(0.93±0.01)	NO	57± 49	108	NO	1.67
5	Plage	(1.02±0.01)	NO	103± 95	199	NO	1.67
6	Plage	1.57±0.02	YES	29 ± 22	50	YES	1.66
7	Plage	1.57±0.02	YES	14 ± 12	26	YES	1.64
8	Plage	1.87±0.03	YES	12 ± 15	28	YES	1.56
9	Plage	1.78±0.02	YES	22 ± 19	42	YES	1.64
10	Sunspot	(0.55±0.01)	NO	233±268	501	NO	1.60
11	Plage	1.58±0.02	YES	16 ± 15	31	YES	1.65
12	Plage	(0.68±0.08)	NO	30 ± 23	54	NO	1.60
	Observations	1.67±0.14					1.60±0.07
	Theory	1.80					1.50

Table 2: Results of 12 datasets obtained with HMI/SDO, including the power law slope α_{F2} of the flux distribution, the maximum flux F_{max}, and fractal dimension D_A. Note that the power law slope α_{F2} agrees with the theoretical prediction of $\alpha_F = 9/5 \approx 1.8$, when there is no sunspot and the magnetic flux is balanced. The values of α_{F2} in parenthesis indicate outliers and are ignored in the averages.

Number Dataset HMI #	Phenomenon	Power law slope fit $\alpha_{\rm F2}$	Matching prediction $\alpha_{\rm F2} \approx 1.8$	Average flux $F_{avg} \pm F_{sig}$ [DN/s]	Magnetic field	Matching balance q_{pos}	Matching balance $q_{pos} \approx 0.50$	Fractal dimension D_A
1	Sunspot	(1.34±0.05)	NO	156±295	+1073	(0.04)	NO	1.54
2	Sunspot	(1.28±0.01)	NO	102±232	-1729	(0.16)	NO	1.55
3	Sunspot	(1.05±0.03)	NO	241±306	-2076	(0.99)	NO	1.59
4	Plage	(1.32±0.02)	NO	63 ±123	+1785	(0.29)	NO	1.58
5	Plage	(1.28±0.02)	NO	67 ±143	-1186	(0.81)	NO	1.57
6	Plage	1.57±0.03	YES	29 ± 69	+1854	0.44	YES	1.51
7	Plage	1.71±0.03	YES	29 ± 70	-1011	0.43	YES	1.51
8	Plage	1.89±0.03	YES	28 ± 73	-1022	0.38	YES	1.49
9	Plage	1.81±0.02	YES	25 ± 65	+955	0.44	YES	1.50
10	Sunspot	(0.96±0.01)	NO	228±326	-1055	(0.34)	NO	1.66
11	Plage	1.79±0.03	YES	29 ± 68	+2058	(0.92)	NO	1.51
12	Plage	(1.29±0.04)	NO	76 ±137	+1036	(0.88)	NO	1.52
	Observations	1.75±0.12				0.42 ± 0.03		1.79±0.07
	Theory	1.80				0.50		1.50

Table 3: Diagram of phenomena observed with different instruments (IRIS, HMI), different wavelengths (columns), for linear and nonlinear random processes (rows).

	IRIS 1400 Å	HMI 6173 Å
linear random process (Gaussian function)	granules	salt-and-pepper small-scale magnetic fields
nonlinear random process (power law function)	spicules	flares, nanoflares magnetic reconnection

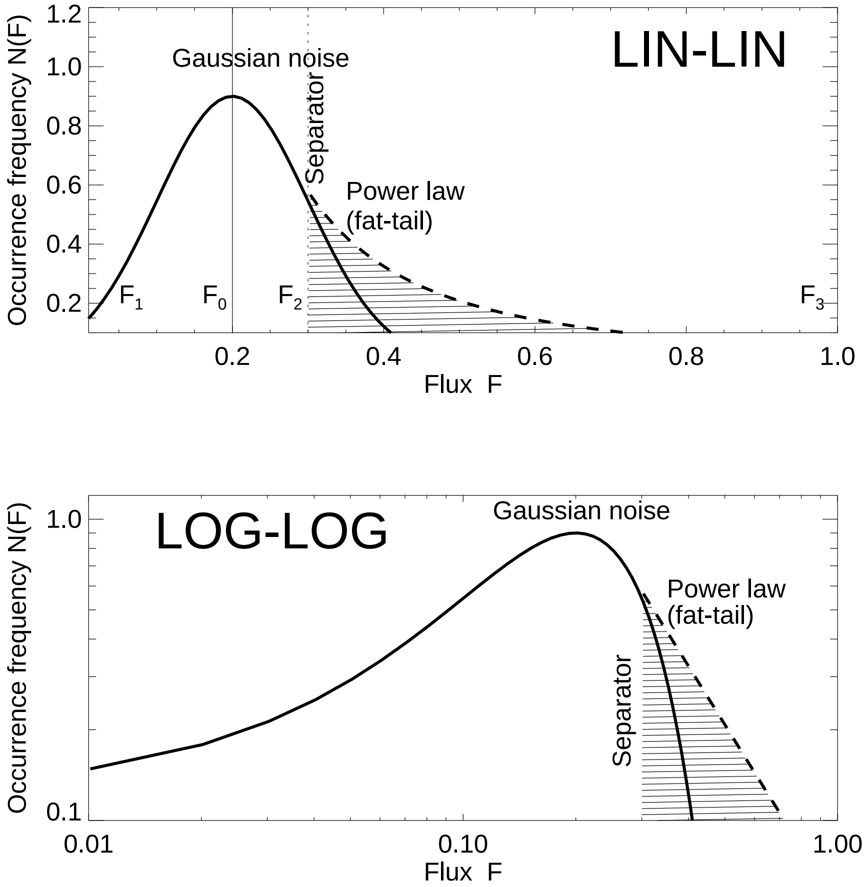

Fig. 1.— A schematic of the two size distributions is shown: a Gaussian function for the linear random statistics, and a power law function (also called fat-tail) for the statistics of nonlinear, avalanching events, separated at a critical value F_2. The upper panel shows a linear (LIN-LIN) representation, the lower panel a logarithmic (LOG-LOG) representation.

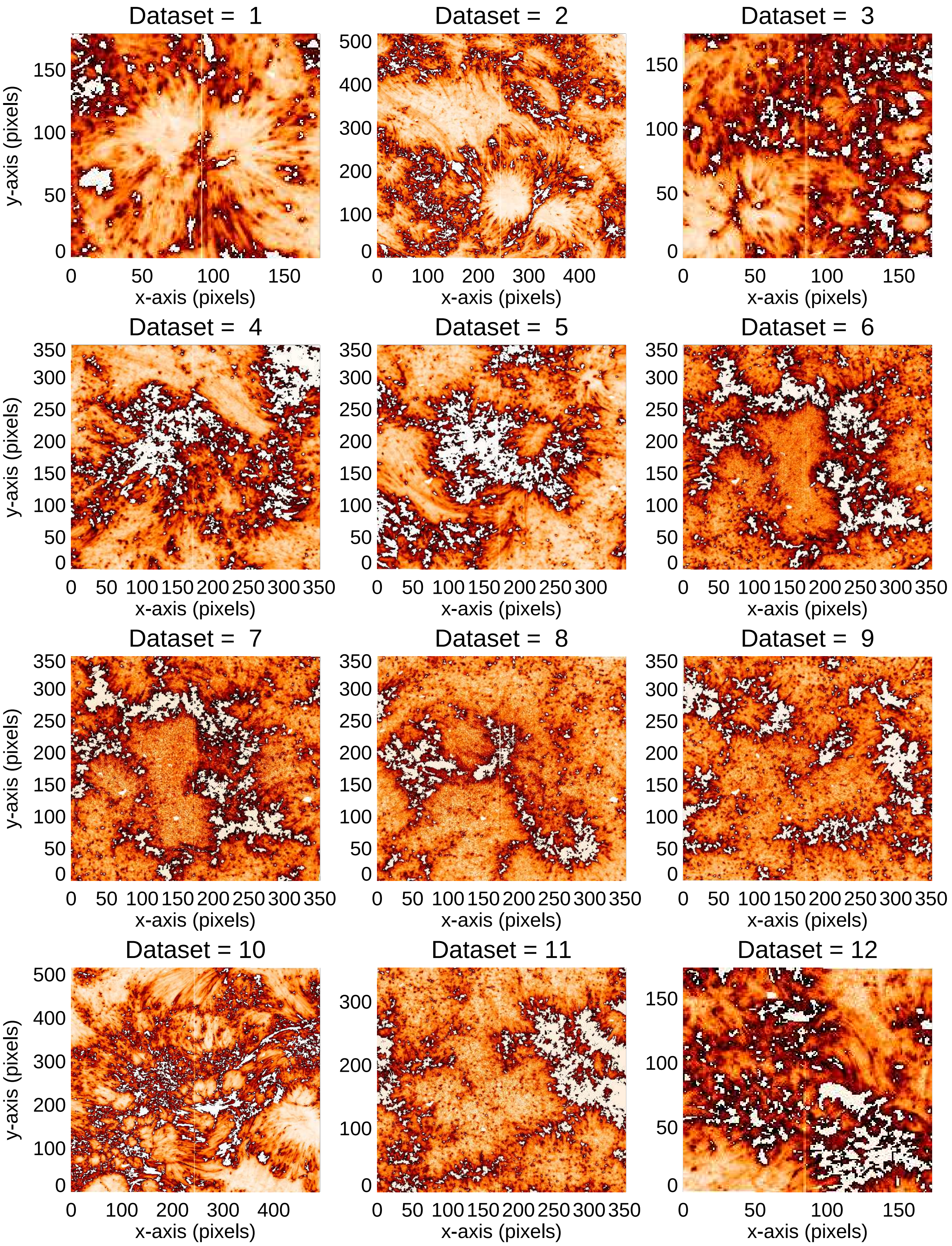

Fig. 2.— Intensity maps of 12 different active regions and Quiet-Sun regions, observed with IRIS SJI 1400 Å. Granules are rendered in orange-to-red color, while spicules and network cells are masked out with white color.

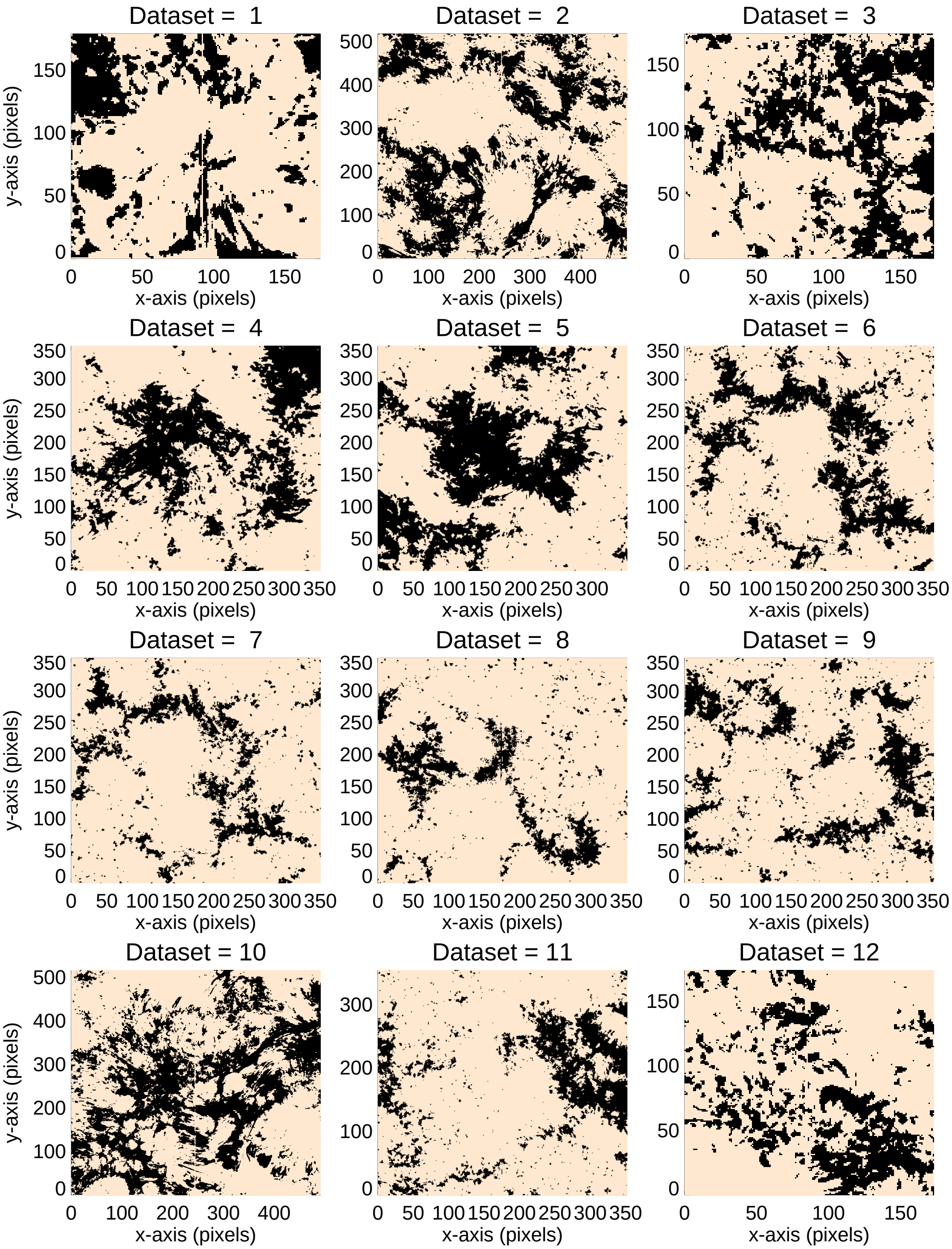

Fig. 3.— Intensity maps of 12 different active regions and Quiet-Sun regions, observed with IRIS SJI 1400 Å. Granular structures are masked out (with peak fluxes $F(x, y) < F_{thr}$), while network cells and spicules are rendered in black.

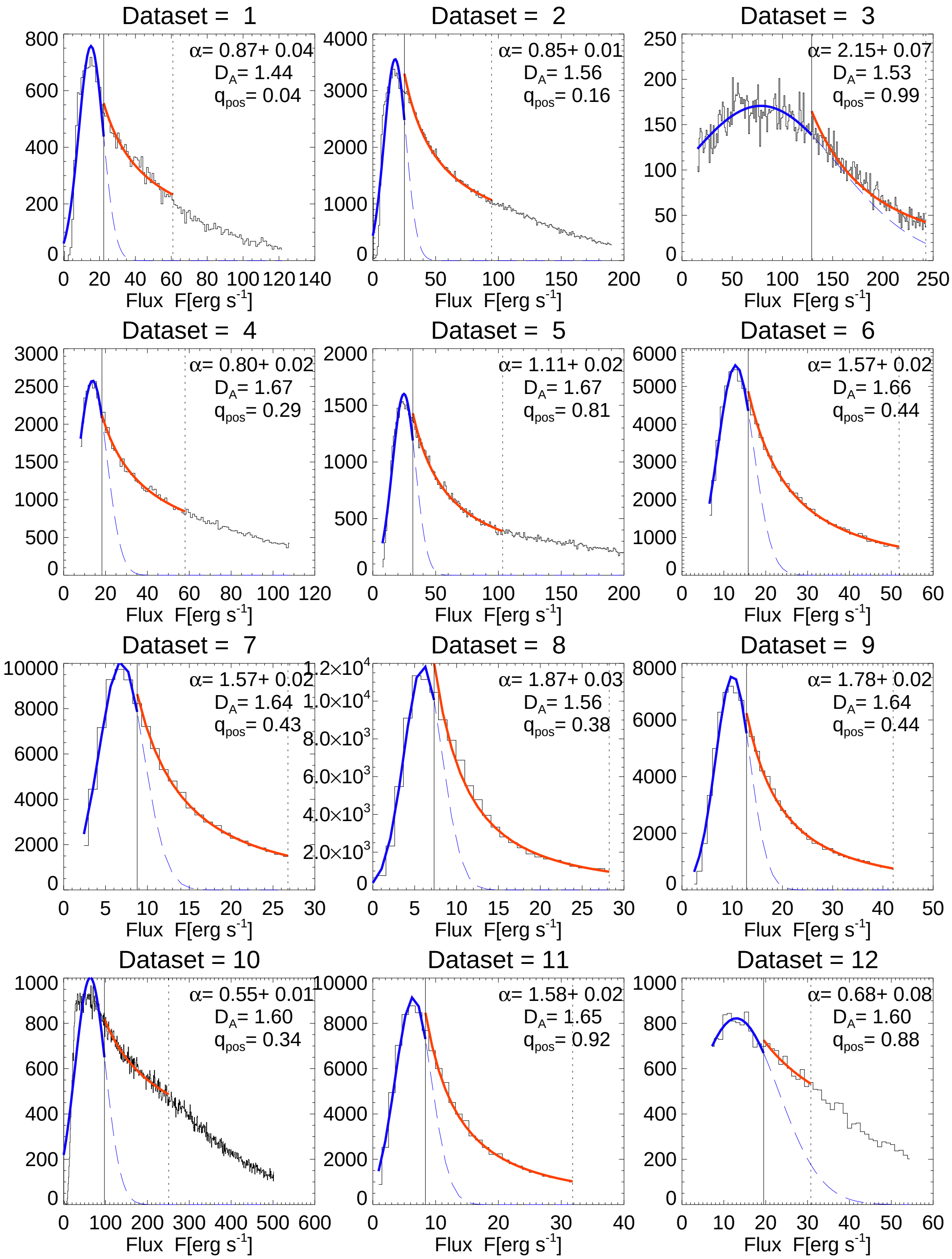

Fig. 4.— Mean flux histograms of 12 different regions in plages of transition regions, observed with IRIS SJI 1400 Å . The flux distribution of granules is fitted with a Gaussian function (blue curve, $F < F_2$), and extrapolated with dashed blue curves. The flux distribution of spicules is fitted with a power law distribution function (thick red curve. The separation between the two distributions is marked with a vertical thin line.

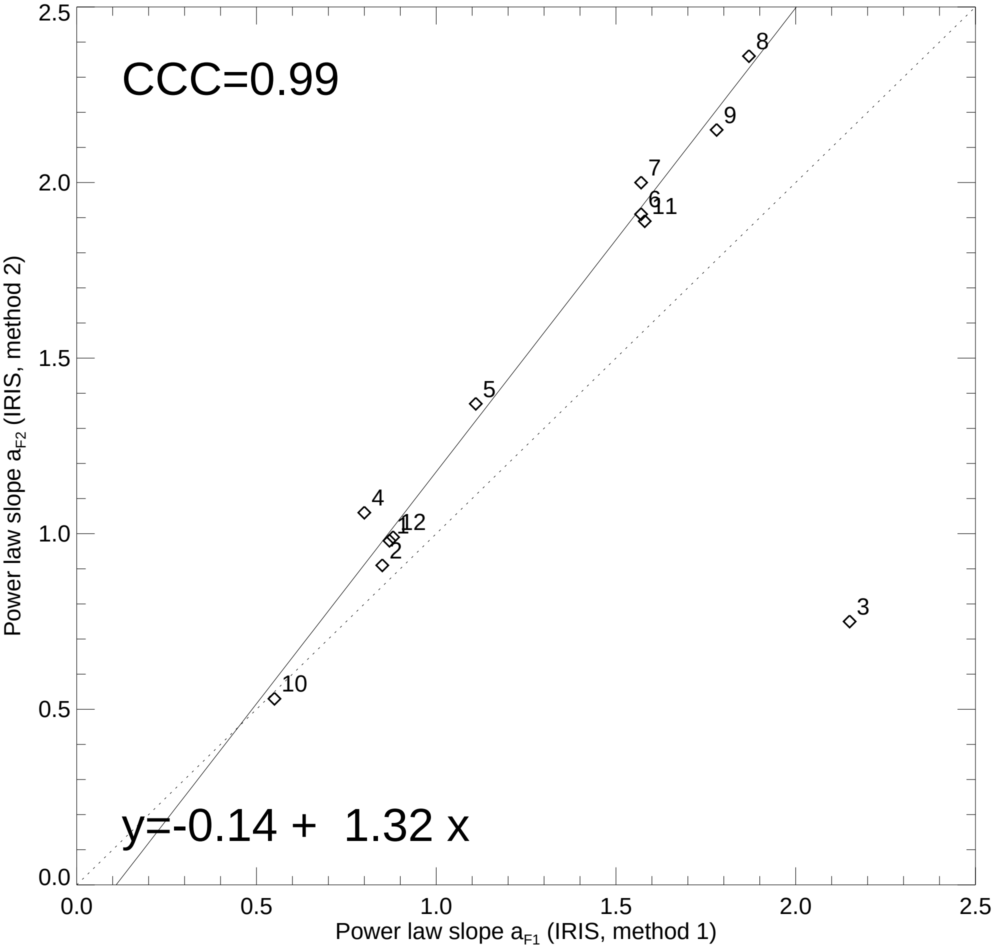

Fig. 5.— Power law index α_F calculated with two different methods of IRIS 1400 Å data: with the all-pixel Method 1 (x-axis), and the peak-pixel Method 2 (y-axis). A linear regression fit is shown (solid line), the cross-correlation coefficient CCC=0.99, the equivalence (dashed diagonal line), and the outlier (# 3) is ignored.

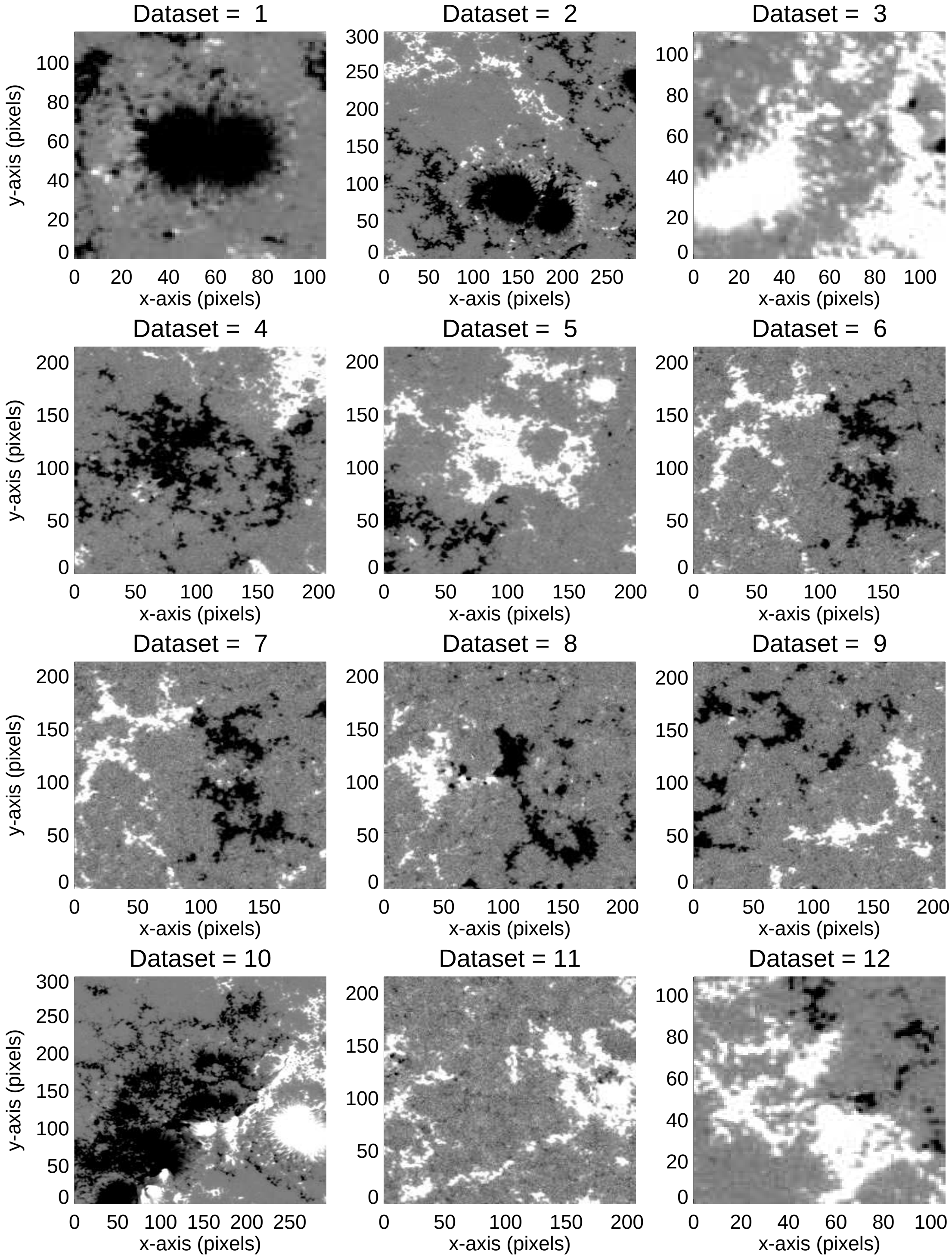

Fig. 6.— Magnetograms of 12 different active regions and plage regions, observed with HMI/SDO . The black color indicates negative magnetic polarity, and the white color indicates positive magnetic polarity.

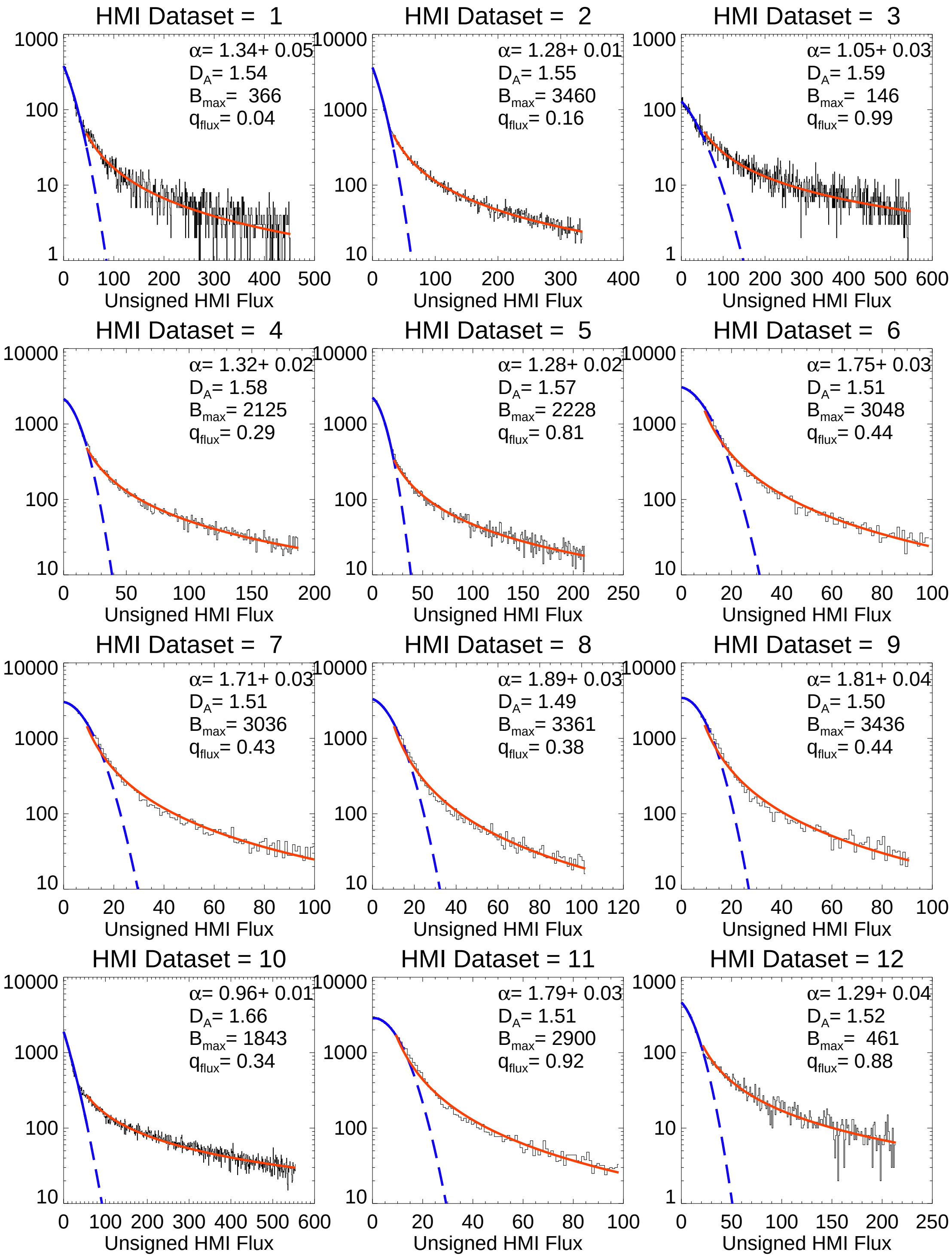

Fig. 7.— Histograms of different solar regions, observed in magnetograms with HMI/SDO. The size distribution of salt-and-pepper magnetic noise is fitted with a Gaussian function (blue curve), while the distribution of magnetic features are fitted with a power function (red curves).

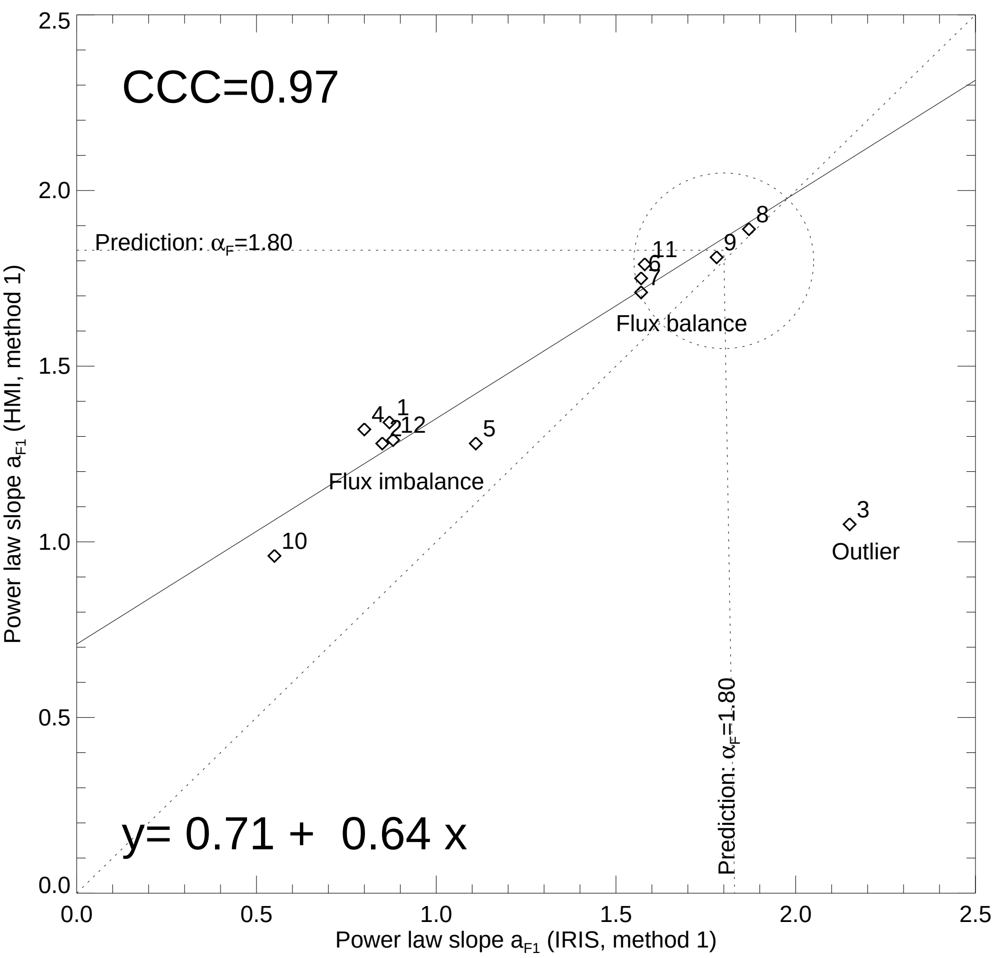

Fig. 8.— Power law slope α_F is calculated for two datasets observed in different wavelengths: from IRIS data (x-axis) and from HMI/SDO data (y-axis). A linear regression fit is shown (solid line), along with the cross-correlation coefficient CCC=0.97, the equivalence (dotted diagonal line), the theoretical prediction $\alpha_F = 1.80$ (vertical and horizontal dotted lines), and the outlier (# 3) is ignored.